IEEE Access
Multidisciplinary ⋮ Rapid Review ⋮ Open Access Journal

Received 6 September 2023, accepted 26 September 2023, date of publication 5 October 2023, date of current version 11 October 2023.

Digital Object Identifier 10.1109/ACCESS.2023.3322281

RESEARCH ARTICLE

W-Band Co-Prime Array FMCW MIMO Radar With IPCE Algorithm for High-Angular Resolution

TAEWOO YU[1], EUNBIN KIM[2], JAE-HYUN PARK[2], (Student Member, IEEE), BYUNG-SUNG KIM[2], (Member, IEEE), AND SANGWOOK NAM[1], (Senior Member, IEEE)

[1]INMC, Department of Electrical and Computer Engineering, Seoul National University, Seoul 08826, South Korea
[2]College of Information and Communication Engineering, Sungkyunkwan University, Suwon 14619, South Korea

Corresponding author: Sangwook Nam (snam@snu.ac.kr)

This research was supported by Unmanned Vehicles Core Technology Research and Development Program through the National Research Foundation of Korea (NRF) and Unmanned Vehicle Advanced Research Center (UVARC) funded by the Ministry of Science and ICT, the Republic of Korea (2020M3C1C1A01084573).

ABSTRACT In recent years, the research on FMCW radar utilizing the mmWave band has gained significant attention, especially in its application to autonomous driving systems. As a potential replacement for lidar, high-resolution studies have been pursued, necessitating large aperture sizes and a considerable number of channels. In this study, high angular resolution is achieved by creating Multiple-Input Multiple-Output (TDM-MIMO) radar system with 6 Tx 8 Rx based on a co-prime array configuration in the W-band. To simplify the interface between the proposed array configuration and the actual chipsets, a 65-nm CMOS process-based single-channel T/Rx chipset with one-to-one aperture coupling to the antenna is employed, minimizing losses, phase deviations, and radiation pattern impacts seen in direct coupling methods using transmission lines in the mmWave band. In addition, the proposed co-prime array exhibits more sidelobe effects, making it challenging to extract actual targets from the angular spectrum. To tackle this, the paper presents the Iterative Peak Component Elimination (IPCE) algorithm, validated through experiments, effectively resolving the issue. The study's findings contribute to advancing high-resolution radar systems, enhancing target detection and tracking capabilities, particularly in automotive radar applications.

INDEX TERMS Co-prime array, FMCW radar, high-resolution, IPCE method, TDM-MIMO.

I. INTRODUCTION

Recent advancements in mmWave technology have sparked significant research and development in FMCW radar, particularly in applications such as autonomous automotive [1], [2], [3], Unmanned Arial Vehicles (UAVs) [4] and imaging [5]. Unlike vision sensors or lidar, radar offers the advantage of target detection even in adverse weather conditions. However, achieving high resolution in radar sensors poses challenges due to their relatively low frequency band [6]. Determining both the distance and angle of a target is critical, with distance resolution determined by signal bandwidth and angular resolution by the aperture's electrical size. Constructing large apertures with physical antennas can be complex and costly. To address this, researchers have explored methods to minimize the number of channels required for high-resolution radar systems.

One approach involves employing the MIMO technique, which allows the creation of virtual arrays, reducing the number of channels while maintaining desired angular resolution [7], [8]. Additionally, diverse array configurations, such as sparse array designs [9], co-prime arrays [10], [11], and nested arrays [12], [13], have been utilized to achieve the same beam width with fewer channels compared to traditional Uniform Linear Array (ULA) methods.

Despite these advances, there are several issues. First, when designing the system with the mentioned array configuration, it is crucial to consider the interface between the chip and the antenna. Implementing direct coupling can lead to lengthening the transmission line or using bending

The associate editor coordinating the review of this manuscript and approving it for publication was Fabrizio Santi.

techniques, which may result in signal amplitude and phase deviations between channels, and even impact the antenna beam pattern. To address this issue, signal excitation methods utilizing the substrate integrated waveguide (SIW) technique or waveguide method have been proposed [14], [15]. Nonetheless, these effects become more pronounced due to the short wavelength, particularly in the mmWave band, and manufacturing challenges arise due to errors in the PCB process [16].

Second, implementing various array configurations can introduce sidelobe issues, including grating lobes rather than ULA structure. This artifact makes it challenging to distinguish signals originating from actual targets and those influenced by sidelobes. In order to solve this problem, many research groups have solved the optimization problem to find the optimal antenna array position, aiming to minimize the Side Lobe Level (SLL) through the utilization of the Array Ambiguity Function (AAF) concept [17], [18]. While this approach provides a solution for reducing SLL in the array design, it inevitably leads to increased system complexity due to intricate array configurations, as highlighted in the preceding paragraph. In other words, when solving optimization problems, careful consideration must be given to the feasibility of system fabrication, potentially necessitating additional constraints. As an alternative approach, various window functions, such as Hamming, Blackman and Spatial Variant Apodization (SVA), can be applied to reduce the SLL [19], [20]. However, when considering angular estimation with co-prime arrays, the dominant sidelobes arise from grating lobes generated by individual virtual arrays. These grating lobes defy attenuation via straightforward window techniques, rendering such methods unsuitable for co-prime array systems.

To address aforementioned issues, the system was designed employing single-channel T/Rx chipsets based on the 65-nm process. By establishing a one-to-one correspondence between the antenna module with a significant separation distance and the single-channel chipset, they effectively resolved the problems and reduced the complexity maintaining the angular resolution performance. In addition, we present a simple signal processing technique to overcome the sidelobe suppression challenges in co-prime array FMCW MIMO radar. Our proposed algorithm aims to distinguish between genuine target signals and sidelobe-induced signals effectively. Measurement results with the implemented system demonstrate successful target differentiation, leading to promising potential for practical applications.

The remainder of the paper is organized as follows: Section II outlines the derivation of array antenna configurations and presents simulation results. Section III describes the overall hardware configuration of the radar system based on simulation data. In Section IV, we introduce the signal processing technique for angle estimation. Section V presents the real measurement results using the system, and finally, we conclude the paper in Section VI, discussing the contributions and future prospects of our proposed approach.

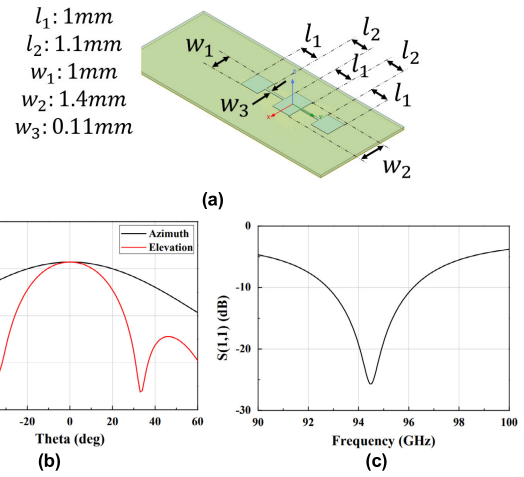

FIGURE 1. Antenna simulation results: (a) antenna geometry, (b) gain pattern result at 94.5 GHz, (c) return loss characteristics.

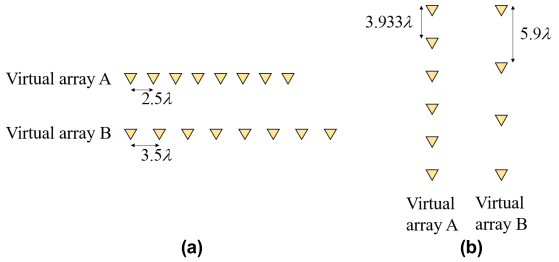

FIGURE 2. Derived virtual array configuration using co-prime array concept: (a) azimuth direction two virtual arrays, (b) elevation direction two virtual arrays.

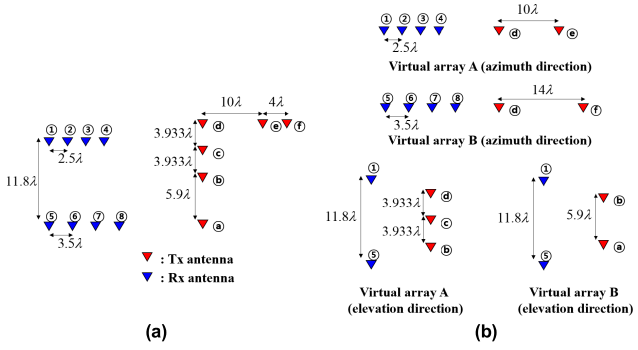

FIGURE 3. Configured real array with TDM-MIMO scheme from derived virtual array: (a) real array configuration, (b) equivalent virtual array.

II. ANTENNA ARRAY CONFIGURATION AND SIMULATION RESULT

In this study, the azimuth and elevation directions are denoted as the xz-plane and yz-plane, respectively. The field of view (FoV) is aimed at ±30° and ±15° for the azimuth and elevation directions, respectively. In order to satisfy the FoV, a series-fed patch antenna with 3 patches is used as a single element [17]. The antenna was designed using RT/Duroid 5880 substrate with a permittivity of 2.2 and a thickness of 0.5 mil. The simulation results of the return loss and

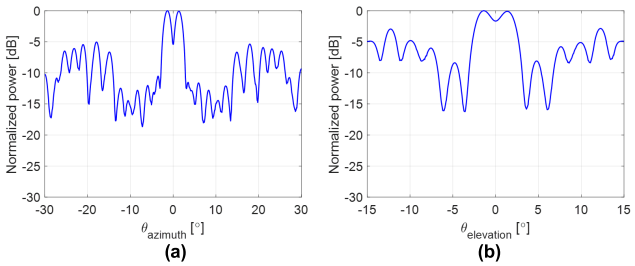

FIGURE 4. Two planewaves incidence simulation DoA result with FFT: (a) Azimuth direction angular estimation result ((+1°, −1°) incidence), (b) Elevation direction angular estimation result ((+1°, −1°) incidence).

beam pattern characteristics at 94.5 GHz are presented in Fig. 1. Half power beam width (HPBW) is 58° and 29° for azimuth and elevation direction, respectively. The impedance matching bandwidth, measured at −10 dB, is 3.35 GHz, and the antenna gain value is 11.7 dBi at 94.5 GHz. The antenna efficiency is determined to 75.2 % at 94.5 GHz.

To achieve high angular resolution, the antenna array is configured using co-prime array technology, which involves implementing two or more ULA with different element spacings [10]. The formation of grating lobes becomes a problem as the element spacing increases, but the grating lobe level can be reduced by obtaining the correlation of two or more patterns with grating lobes formed at different angles [11]. Therefore, a sharp array pattern with a small number of channels can be obtained by employing several ULA designs with appropriate spacings and the number of elements. In this study, a parameter sweep method is employed to derive the element spacing and number of elements, taking into account the physical dimension of the single antenna element. The aperture sizes of each virtual array are 24.5λ and 19.7λ for azimuth and elevation direction, respectively. Theoretically, without considering the antenna element pattern, the angular resolution is calculated with the following equation:

$$\Delta\theta \approx \frac{\lambda}{(N-1)\,d} \tag{1}$$

where N and d is the number of antenna and element spacing, respectively. From (1), the angular resolution can be calculated to 2.37° and 2.91°, respectively. The derived array virtual array is shown in Fig.2. In order to implement the derived virtual ULAs with a smaller number of channels as a real array, TDM-MIMO method is adopted. By using the MIMO technique, a virtual array can be formed in the form of a convolution of a Tx antenna and an Rx antenna [7], [8]. Fig.3 shows the configured real array with TDM-MIMO method.

However, despite expecting grating lobe suppression effects, proper sidelobe suppression outside the main lobe region is not achieved. This phenomenon becomes more pronounced when distinguishing between multiple planewaves using this antenna array, and this issue is evident from the simulation results. In the MATLAB simulations, we set the SNR to 10 dB in a white Gaussian noise environment, with 80 snapshots. The incidence angles of two plane waves are set to (+1°, −1°) for both azimuth and elevation direction. As shown in Fig.4, sidelobes are observed at levels close to 0 dB, making it challenging to distinguish the direction of the actual incident planewave or identify the spurious components based on this beam pattern.

In this paper, we introduce an algorithm to address this problem, which is presented in the following section. The algorithm aims to resolve the issues with sidelobe suppression, enabling accurate identification of the actual incident planewave and discriminating against false signals.

III. ITERATIVE PEAK COMPONENT ELIMINATION (IPCE) TECHINQUE

A. ALGORITHM DESCRIPTION

The signals received from each virtual array can be mathematically expressed as:

$$\boldsymbol{y}_1 = \boldsymbol{A}_1\mathbf{s} + \mathbf{n} \tag{2}$$

$$\boldsymbol{y}_2 = \boldsymbol{A}_2\mathbf{s} + \mathbf{n} \tag{3}$$

where $\mathbf{A}_1$,$\mathbf{A}_2$, $\mathbf{s}$ and $\mathbf{n}$ are steering matrix for virtual array 1 and 2, signal vector and noise vector, respectively. The conventional approach involves deriving the angular spectrum by processing the received signals from individual virtual arrays and then performing correlation to obtain the angle spectrum. In this paper, we present a signal processing technique that directly utilizes this conventional angle spectrum. One critical assumption is that the magnitude of the signals returning from the main lobe, caused by the target, is always greater than the combined magnitude of signals formed by sidelobes. According to this assumption, the peak point in the resulting original spectrum corresponds to a definite target angle, which we denote as θ_1. Assuming the incidence of a single planewave at θ_1, we can derive artificially the received signal vector at each virtual array, utilizing (2) and (3). By subtracting the newly obtained virtual received signal vector from each respective original received signal, the re-modeled received signals from each virtual array as follows:

$$\boldsymbol{y}_{1\_iter1} = \boldsymbol{y}_1 - \boldsymbol{a}_1(\theta_1)s_{11} \tag{4}$$

$$\boldsymbol{y}_{2\_iter1} = \boldsymbol{y}_2 - \boldsymbol{a}_2(\theta_1)s_{21} \tag{5}$$

where s_{11} and s_{21} represent the phasor of the incident signal from θ_1 in the reference channel of each virtual array. The newly modeled signals, $\boldsymbol{y}_{1\_iter1}$ and $\boldsymbol{y}_{2\_iter1}$, have removed the influence of the target incident at θ_1. By utilizing these signals, we can reconstruct the angular spectrum, excluding the component corresponding to the incident angle θ_1. Performing correlation on this reconstructed spectrum allows us to identify the remaining components apart from θ_1, denoted to the residual angular spectrum. During this process, we again search for the angle information corresponding to the peak value, and let this angle be denoted as θ_2. The equivalent received signals, after removing the component corresponding to θ_2, can be expressed using the following equation:

$$\boldsymbol{y}_{1\_iter2} = \boldsymbol{y}_{1\_iter1} - \boldsymbol{a}_1(\theta_2)s_{12} \tag{6}$$

Algorithm 1 IPCE Method

Input: $P(\theta) = \sqrt{P_1(\theta) P_2(\theta)}$

Output: $\theta_1, \theta_2, \theta_3, \ldots, \theta_k$

Initialization:

Calculate angular spectrum for each virtual array

Calculate total angular spectrum with geometric mean

$$P(\theta) = \sqrt{P_1(\theta) P_2(\theta)}$$

while

Find peaks and index of $P(\theta)$: θ_{peak}

Subtract the θ_{peak} effect from the received signal for each virtual array

$$\boldsymbol{y}_{1\_iter1} = \boldsymbol{y}_1 - \boldsymbol{a}_1(\theta_{peak}) s_{1peak}$$
$$\boldsymbol{y}_{2\_iter1} = \boldsymbol{y}_2 - \boldsymbol{a}_2(\theta_{peak}) s_{2peak}$$

Calculate $P_{iter}(\theta)$

if $\max(P(\theta))$- $\max(P_{iter}(\theta)) <$ dynamic range of the system

Stop iteration

end if

end while

Formulate $k \times k$ inverse problem for each virtual array

Solve the inverse problem to find the signal's amplitude

Re-calculate final angular spectrum:

$$P_{final}(\theta) = \sqrt{P_{1\_final}(\theta) P_{2\_final}(\theta)}$$

$$\boldsymbol{y}_{2\_iter2} = \boldsymbol{y}_{2\_iter1} - \boldsymbol{a}_2(\theta_2) s_{22} \tag{7}$$

where s_{12} and s_{22} represent the phasor of incident signal from θ_2, similar to the above expressions. Throughout this iterative process, we repeated the procedure to remove the angle corresponding to the peak point one by one. The number of iterations is determined by monitoring the difference in peak magnitudes between the residual angular spectrum generated through successive iterations and the original initial spectrum. If this difference becomes larger than the system's dynamic range, the iteration step is terminated.

However, it should be noted that the complex values representing the signals at each angle on the already derived original spectrum may not be entirely accurate due to the influence of added sidelobes. Consequently, to precisely determine the magnitude of the incident signals at the estimated angles obtained in the above process, additional calibration is necessary. Assuming that the number of actual detected targets is k, the following equation can be used for amplitude calibration:

$$\hat{s}_1 = \widehat{\boldsymbol{A}_1^H} \widehat{\boldsymbol{A}_1} \boldsymbol{s}_1 \tag{8}$$
$$\hat{s}_2 = \widehat{\boldsymbol{A}_2^H} \widehat{\boldsymbol{A}_2} \boldsymbol{s}_2 \tag{9}$$

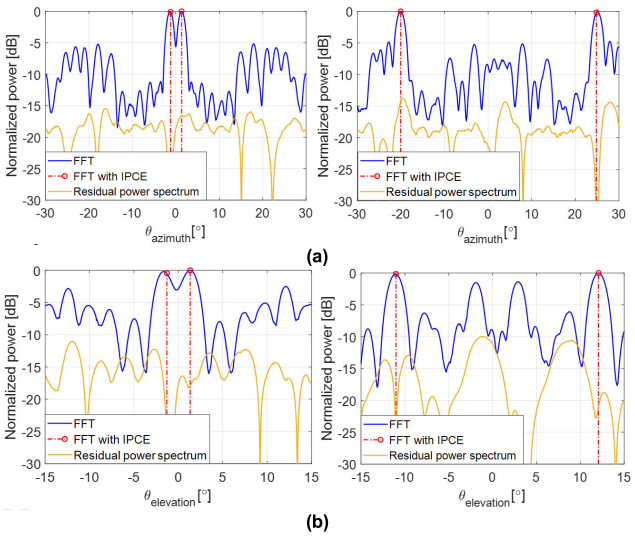

FIGURE 5. Two planewaves incidence simulation DoA result with the IPCE: (a) Azimuth direction angular estimation result (simulation setup: left: (+1°, −1°) incidence, right: (−20°, +25°) incidence, IPCE result: left: (+1.24°, −1.2°), right: (−19.8°, +25.07°)), (b) Elevation direction angular estimation result (simulation setup: left: (+1°, −1°) incidence, right: (−11°, +12°) incidence, IPCE result: left: (1.32°, −1.12°) incidence, right: (−11.06°, +12.06°)).

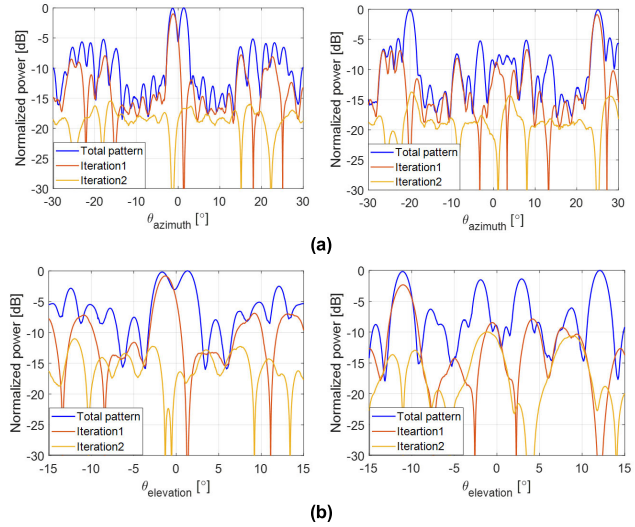

FIGURE 6. Residual angular spectrum for each iteration: (a) Azimuth direction angular estimation result (left: Fig.5(a) left, right: Fig.5(a) right), (b) Elevation direction angular estimation result (left: Fig.5(b) left, right: Fig.5(b) right).

where

$$\widehat{\boldsymbol{A}_1} = [\boldsymbol{a}_1(\theta_1), \boldsymbol{a}_1(\theta_2), \ldots, \boldsymbol{a}_1(\theta_k)]^T \tag{10}$$
$$\widehat{\boldsymbol{A}_2} = [\boldsymbol{a_2}(\theta_1), \boldsymbol{a}_2(\theta_2), \ldots, \boldsymbol{a_2}(\theta_k)]^T \tag{11}$$
$$\boldsymbol{s}_1 = [s_{11}, s_{12}, \ldots, s_{1k}]^T \tag{12}$$
$$\boldsymbol{s}_2 = [s_{21}, s_{22}, \ldots, s_{2k}]^T. \tag{13}$$

From the above equations, performing the inverse operation of size $k \times k$ for each virtual array allows for more accurate determination of the signal's magnitude arriving

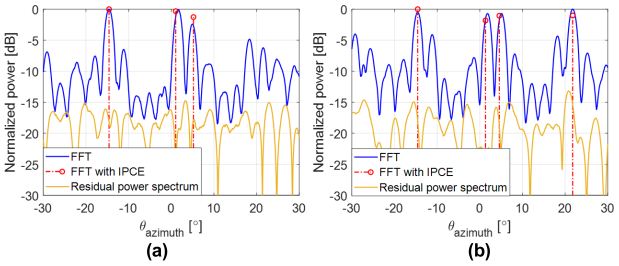

FIGURE 7. Multiple planewaves incidence simulation DoA result with the IPCE for the azimuth direction: (a) three planewaves incidence case (simulation setup: (−15°, +2°, +5°) incidence, IPCE result: (−14.6°, +1.05°, +5.23°)) (b) four planewaves incidence case (simulation setup: (−15°, +2°, +5°, +22°) incidence, IPCE result: (−14.56°, +1.37°, +4.64°, +21.76°)).

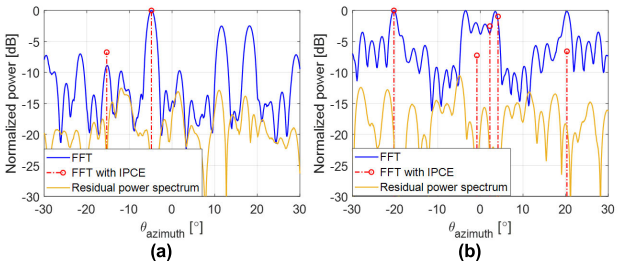

FIGURE 8. Examples showing suboptimal performance of the IPCE: (a) overlapping grating lobe case (simulation setup: (−5°, +12°, +18°) incidence) (b) point cloud distribution target case (simulation setup: (−3°, −1°, +1°, 3°) incidence).

from the derived direction. By obtaining the direction information and magnitudes from each array, a final angle spectrum can be derived by correlating two results as follows:

$$P_{final}(\theta) = \sqrt{P_{1\_final}(\theta)\, P_{2\_final}(\theta)} \tag{14}$$

where $P_{1\_final}(\theta)$ and $P_{2\_final}(\theta)$ are the IPCE results after solving the inverse problem for virtual array 1 and 2, respectively.

B. MULTIPLE TARGET SIMULATION

In order to validate the algorithm following the same simulation setup as before, MATLAB simulation is performed. Simulations are conducted for both azimuth and elevation direction, considering two different scenarios for each. For the azimuth direction, incident angles of two plane waves are set to $(+1°, -1°)$ and $(-20°, +25°)$. As for the elevation direction, we simulated incidents at $(+1°, -1°)$ and $(-11°, +12°)$. The results are depicted in Fig.5, where the effectiveness of the algorithm in accurately detecting real targets amidst a challenging spectrum with poor target discrimination is demonstrated.

In addition, Fig.6 illustrates the power patterns derived at each iteration step, showing the differences in peak values between the original spectrum and the spectrum calculated after each iteration. For all case of Fig.5 and 6, the iteration is repeated twice. This difference is computed at every step and compared with the system's dynamic range; if it exceeds

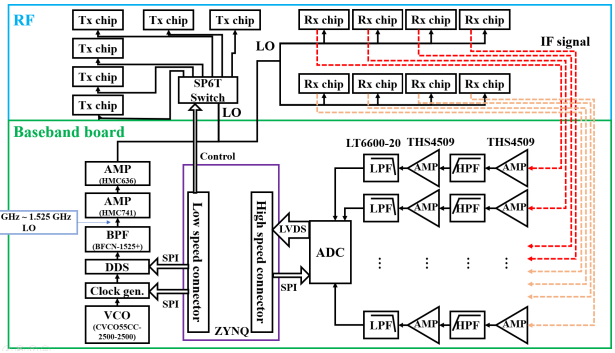

FIGURE 9. Entire radar system block diagram.

the dynamic range, the iteration process is terminated. Upon analysis of the simulation results, it becomes evident that the IPCE algorithm can effectively differentiate between two distinct targets in terms of their azimuth and elevation angles, even when confronted with intricate results from array signal processing.

To validate the algorithm's effectiveness in scenarios involving more than two targets, simulations were conducted. An illustrative example for azimuthal direction is depicted in Fig.7. Fig.7(a) and (b) present simulation results considering the presence of three and four incident planewaves, respectively. The incident angles of multiple planewaves in Fig.7(a) are $(-15°, +2°, +5°)$. Similarly, they are set to $(-15°, +2°, +5°, +22°)$ for Fig.7(b). As evident from the outcomes, the IPCE algorithm exhibits the capability to accurately discern real targets even more intricate spectral environments. The algorithm showcases its proficiency in effectively detecting real targets, as demonstrated by the results obtained from these simulations.

C. LIMITATION OF THE IPCE ALGORITHM WITH CO-PRIME ARRAY

In the previous paragraphs, various planewave incidence simulations were presented to establish the validity of the IPCE algorithm. However, it should be noted that the algorithm's robustness is not universally assured as it relies on the assumption that the magnitude of the signals returning from the main lobe, caused by the target, is always greater than the combined magnitude of signals formed by side lobes or grating lobes. Therefore, configuring specific incident angles for planewaves can lead to diminished confidence in the angle results obtained through the IPCE in simulation. Fig.8(a) and (b) show the angular estimation result with the IPCE method for the specific cases within the given co-prime array configuration. Incident angles of multiple planewaves are set to $(-5°, +12°, +18°)$ for Fig.8(a) and $(-3°, -1°, +1°, +3°)$ for Fig.8(b). This phenomenon arises due to challenges in accurately identifying peak points within the original spectrum or the iteratively evolving residual spectrum. Overlapping grating lobes (e.g. grating lobe + main lobe or grating lobe + grating lobe) from various directions

TABLE 1. T/Rx characteristics.

Chipset	Description	Value
Tx	Maximum transmitted RF power	9.77 dBm
	3 dB bandwidth of the Tx	7.875 GHz (90.72 ~ 98.595 GHz)
	Power consumption of Tx	177.6 mW
Rx	Rx conversion gain	26.2 dB (94.5 GHz)
	3 dB bandwidth of the Rx	3.15 GHz (93.24 ~ 96.39 GHz)
	Power consumption of Rx	142.8 mW

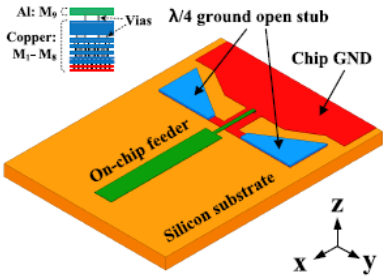

FIGURE 10. On-chip feeder and ground open stub structure on a silicon substrate.

of planewave incidence on the virtual array, coupled with the main signal, can lead to errors during the peak index extraction process. To mitigate these challenges, meticulous design of a co-prime array is essential to prevent overlapping grating lobes, even in complex environments.

Furthermore, another issue arises with the IPCE method when the target is densely clustered in point cloud form. Fig. 8(b) shows the 4 closely spaced planewaves incidence simulation results. Not only the similar issue about grating lobes, but also combinations of the main lobe and adjacent sidelobes can introduce errors in peak index detection, resulting in inaccuracies in extracted angles during the iteration process. Consequently, counterexamples that defy the assumption of the IPCE algorithm, described in the previous paragraph, can emerge. These inherent limitations in the algorithm's performance highlight the need for future research endeavors aimed at overcoming these challenges. This direction is marked as future work, signifying a pathway towards enhancing the algorithm's robustness and accuracy.

IV. RADAR SYSTEM CONFIGURATION

The entire system consists of three parts: Front-end module combined with RF chipset and antenna, baseband module, and ZYNQ board for data transmission to host PC. Fig.9 shows the overall system block diagram.

A. ANTENNA ARRAY AND RF T/RX MODULE

As highlighted in the introductory section of this paper, designing a feeding structure in the mmWave band presents significant challenges. Specifically, the excitation structure for the antenna array, based on the co-prime array discussed

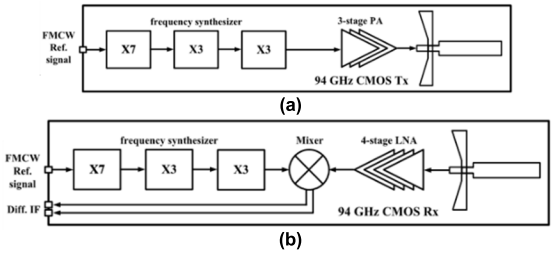

FIGURE 11. T/Rx chip block diagram: (a) Tx, (b) Rx.

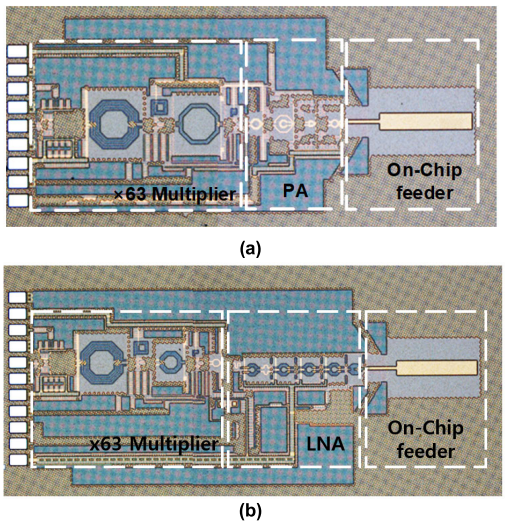

FIGURE 12. Chip micrograph: (a) Tx chipset, (b) Rx chipset.

TABLE 2. System parameters.

Parameters	Value	Description
T_{chirp}	50 µs	Chirp time
P_t	8 dBm	Transmit RF power
BW	1.575 GHz	RF signal bandwidth
G_t	10 dBi	Tx antenna gain
G_r	10 dBi	Rx antenna gain
N	480 80 / single Tx	Total number of chirps
σ	11 dBsm	RCS of corner reflector
F_s	50 MSPS	ADC sampling frequency

in section II, becomes even more intricate to design due to the increased element spacing. Therefore, a single channel T/Rx chipset is used for a single antenna, and each chipset is attached to the back of each antenna for excitation through the aperture coupled feeding method with on-chip feeder [21].

Fig.10 shows the on-chip feeder structure. The structures of T/Rx chipsets, shown in Fig.11, are similar architecture as that presented in the previous work and have been redesigned for operation in the 94 GHz band [21]. Each T/Rx chipset has a built-in ×63 frequency multiplier and generates 94.5 GHz to 96.075 GHz transmit RF signals and LO signals for down conversion, respectively, using reference signals received from 1.5 GHz to 1.525 GHz. Given that the frequency range

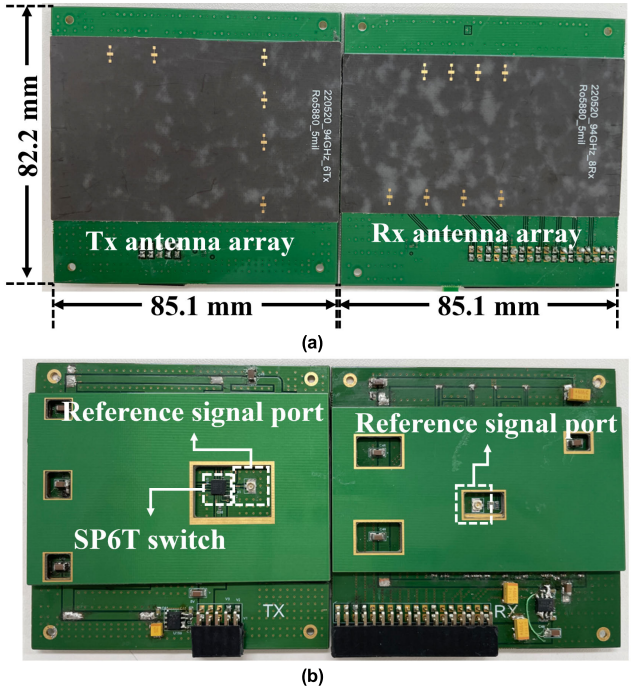

FIGURE 13. RF T/Rx module: (a) front-view, (b) back-view.

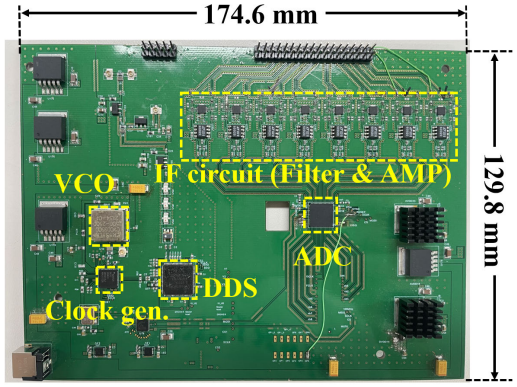

FIGURE 14. Baseband board.

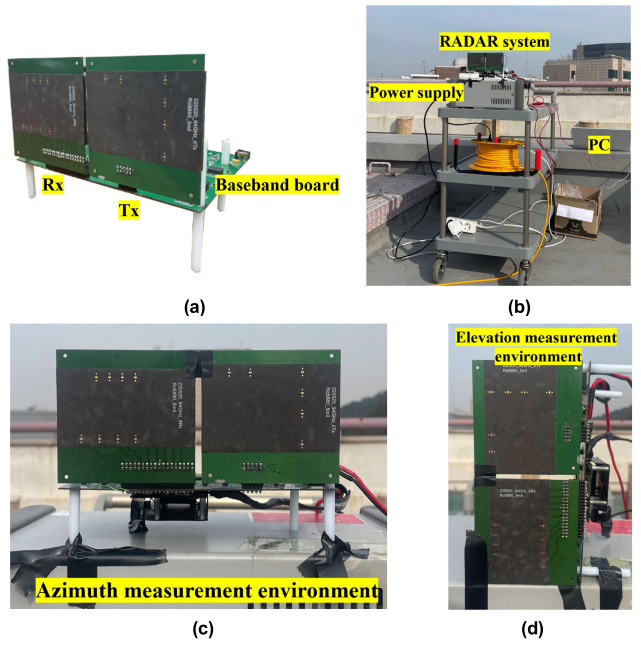

FIGURE 15. Implemented radar sensor: (a) integrated radar system, (b) measurement setup, (c) measurement environment for azimuth angle estimation, (d) measurement environment for elevation angle estimation.

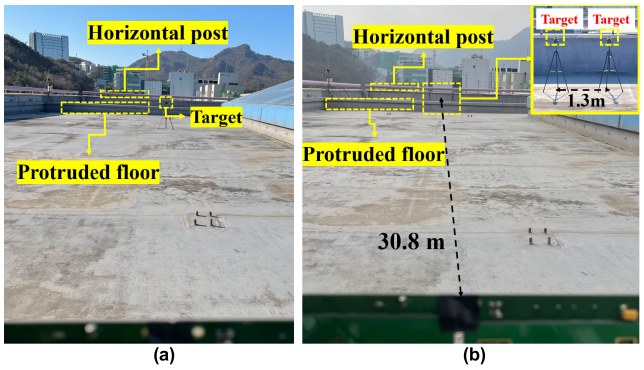

FIGURE 16. Measurement scenario: (a) single target case, (b) two-targets case.

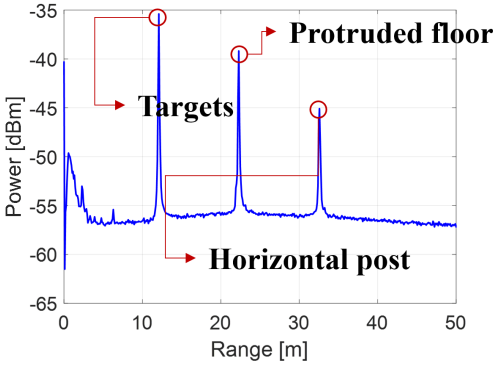

FIGURE 17. Range profile of the single target measurement.

of the reference signal is comparatively lower than that of the transmitted chirp signal, the signal loss caused by the substrate is relatively minimal. Consequently, the routing of the reference signal is carried out on the FR4 substrate. Fig. 12 shows the micrograph of the implemented T/Rx chipsets and the characteristics of the chipsets are introduced in Table 1. The bias and signal lines of the T/Rx chipset attached to the back of each antenna are connected through wire bonding technique.

Fig.13(a) and (b) show the front-view and back-view of the RF T/Rx module, respectively. As shown in Fig. 13(b), a SP6T switch (QPC6064) is included in the board to fit 6 Tx for implementing TDM-MIMO scheme.

B. BASEBAND BOARD WITH SOURCE

The baseband board is made up of three parts: IF circuit & ADC part, FMCW source part, and the embedded board part, as shown in Fig.14. The IF circuit includes a low-pass filter to reduce direct coupling, a high-pass filter to prevent aliasing,

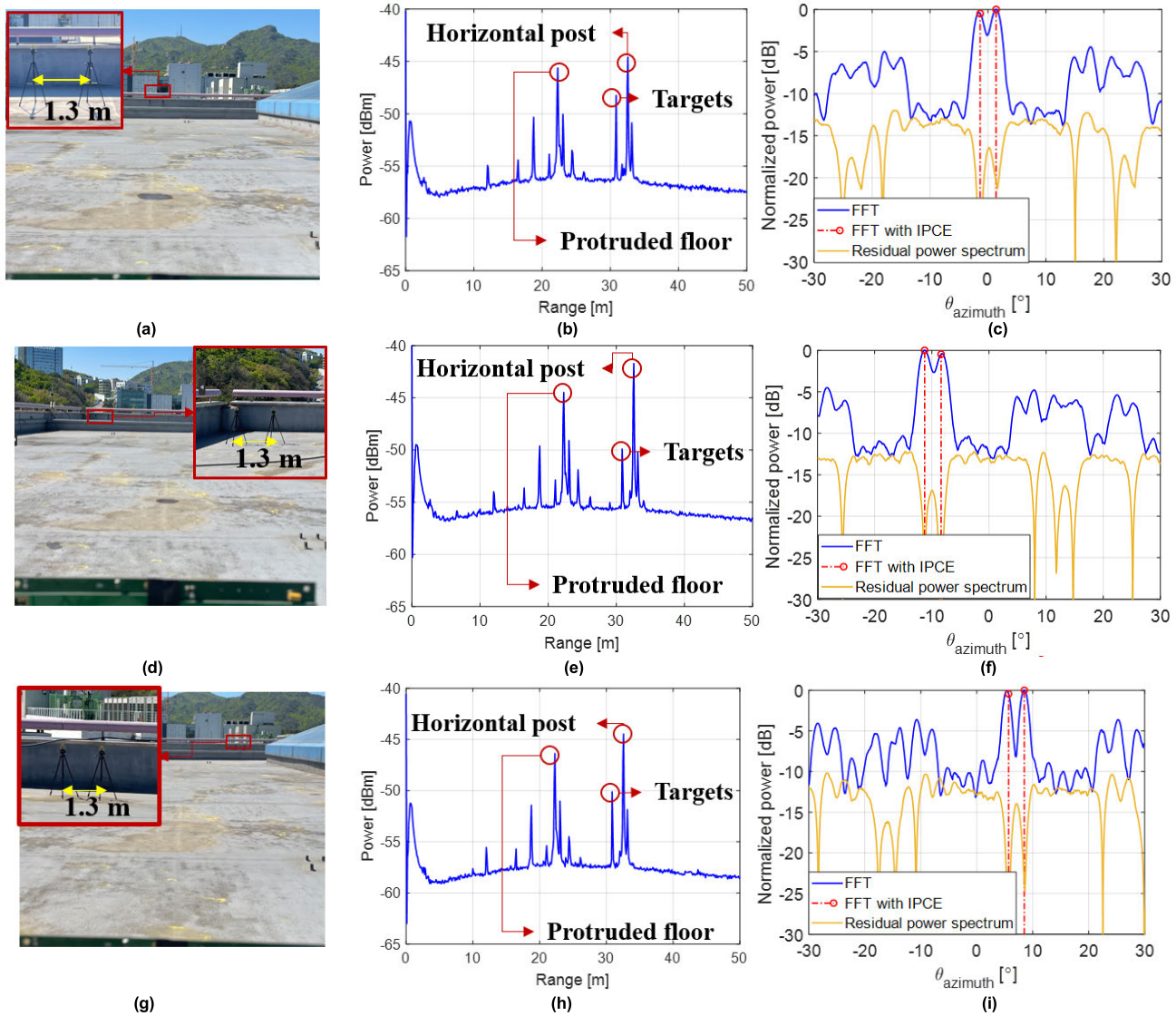

FIGURE 18. Azimuth measurement results: (a) two targets on broadside direction, (b) range profile, (c) angle estimation result at the target index (peak angle: −1.35° and 1.40°), (d) two targets on left side, (e) range profile, (f) angle estimation result at the target index (peak angle: −11.26° and −8.38°), (g) two targets on right side, (h) range profile (i) angle estimation result at the target index (peak angle: 5.68° and 8.50°).

and a gain block. To digitize the signal received from 8 Rx channels simultaneously, the board uses an 8-channel ADC (Texas instrument AFE5801) whose maximum sampling frequency is 65 MSPS. The sampled data is transferred to the embedded board through a low voltage difference signal (LVDS) interface. The clock generator (Analog devices AD9525) generates two clocks for digital direct synthesizer (DDS) (Analog devices AD9915) operation and ADC sampling, and provides the reference clock signal. The DDS generates the reference signal (1.5 GHz ∼ 1.525 GHz), which is then amplified and divided into two paths for the RF Tx and Rx modules. Finally, ZYNQ MPSOC (Avnet Ultra96) is used as the embedded board. Inside the FPGA, some digital logics are implemented including FIFO and timing control. On the processor part, firmware is implemented including SPI configuration, for setting up the clock generator, DDS and ADC, and data refining and transmission to the host PC.

V. MEASUREMENT

Fig.15(a) shows the implemented radar system. Two corner reflectors (SAJ-043-S1) whose RCS value is 11 dBsm were used in the experiment. To check the angle estimation performance of the fabricated system, the experiment was performed by placing the target arrangement left and right while maintaining the separation distance. In addition, check the angular resolution performance for both azimuth and elevation direction, the platform is set as Fig.15(c) and (d).

A. SINGLE TARGET MEASUREMENT

First, single target measurement was completed to check RF link budget and radar range equation. Fig.16(a) illustrates the

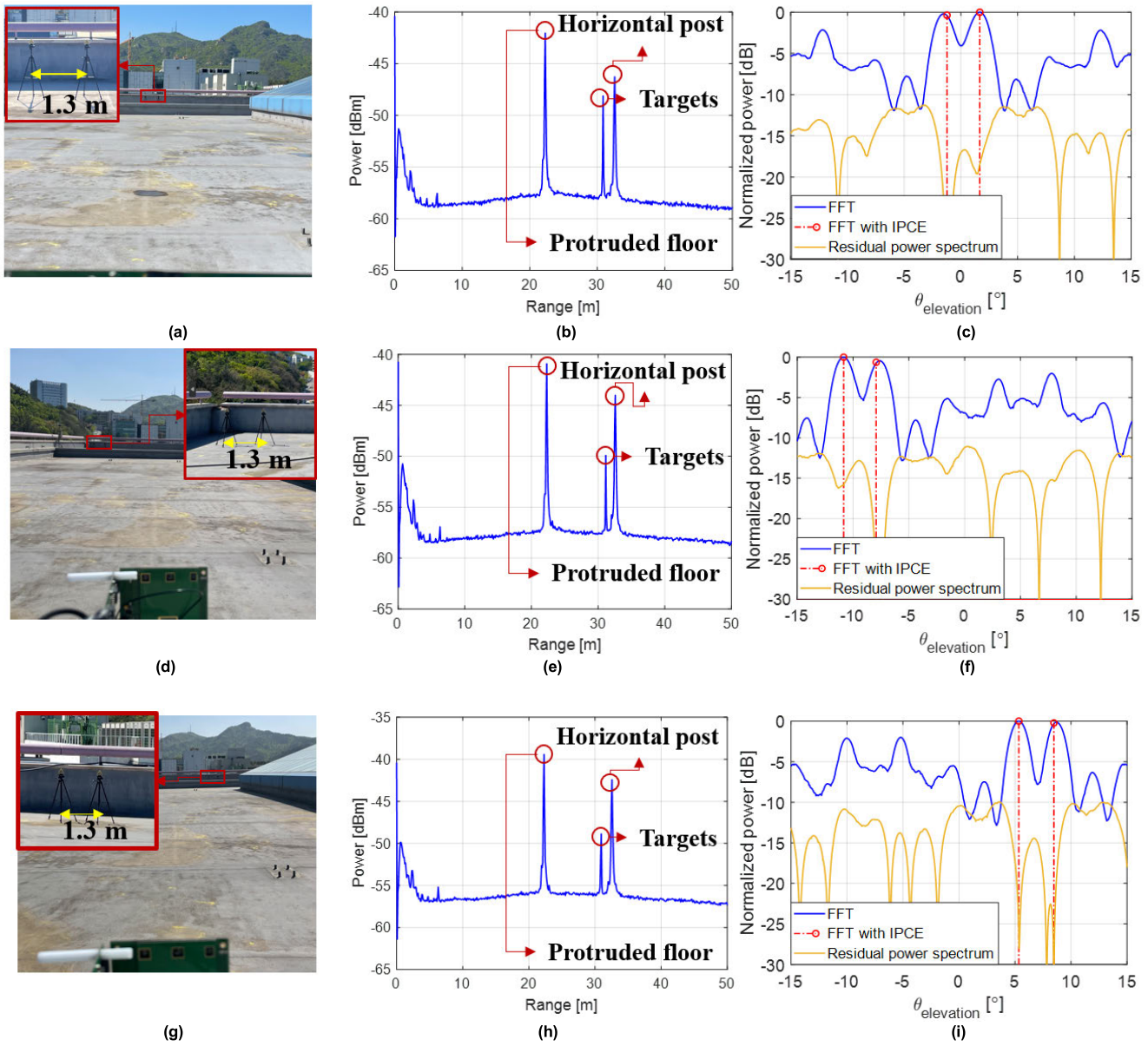

FIGURE 19. Elevation measurement results: (a) two targets on broadside direction, (b) range profile, (c) angle estimation result at the target index (peak angle: −1.23° and 1.66°), (d) two targets on left side, (e) range profile, (f) angle estimation result at the target index (peak angle: −10.85° and −7.93°), (g) two targets on right side, (h) range profile, (i) angle estimation result at the target index (peak angle: 5.34° and 8.47°).

single target measurement scenario. The target is placed at the broadside direction with 12.12 m distance. The estimated range is 12.095 m and the measured SNR is 22.003 dB, shown in Fig.17. The measurement system parameters are outlined in Table 2. Considering the actual chip-to-antenna coupling loss, the estimated gain value for the T/Rx antenna was set to 10 dBi. When these parameters are applied to the radar range equation, the calculated SNR is approximately 25.574 dB, with 15 dB noise figure of the receiver. This value exhibits an approximate 3 dB deviation from the measured result, which can be attributed to potential systematic losses, such as variation in antenna efficiency with frequency, transmission line loss of the reference signal on the FR4 substrate, higher aperture coupling loss than estimated due to on-chip feeder-to-aperture misalignment, and switching loss. The slight increase in power level within the nearby range of 0 to 5 meters represents background noise, including T/Rx direct coupling. In this system, 80 chirp signals were transmitted per each Tx channel, and signal processing was conducted for each individual snapshot. These considerations underlie the selection of the simulation parameters discussed in section II and III, specifically an SNR of around 10 dB and 80 snapshots.

B. TWO TARGETS FOR AZIMUTH DIRECTION

The distance from the radar and the distance between the two targets are set to 30.8 m and 1.3 m, respectively, as shown in Fig.16(b). Fig.18 represents the measurement results for

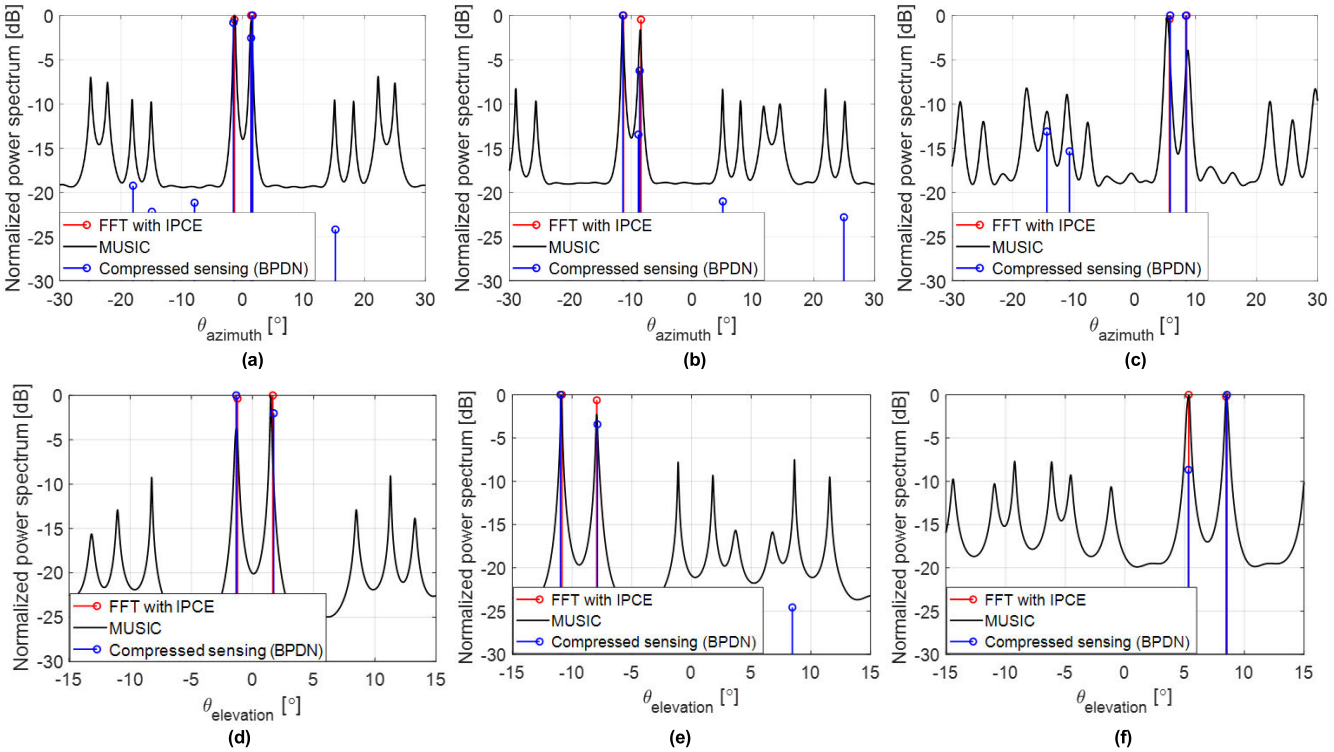

FIGURE 20. Algorithm comparison (FFT with IPCE, MUSIC and compressed sensing (BPDN)): (a) azimuth broadside direction, (b) azimuth left side, (c) azimuth right side (d) elevation broadside direction, (e) elevation left side and (f) elevation right side.

the azimuth direction. Fig.16(a) shows the scenario when two targets are placed at the broadside direction. Fig.18(b) and (c) show the range profile and angular estimation result with the IPCE method in the target's range-bin in the corresponding scenario, respectively. From the range profile, some clutters exist including the scattered approximately 10 dB from the range profile. In this range bin, two peak angles are derived to $-1.35°$ and $1.40°$ (difference: $2.75°$) with the IPCE method. From the ground truth data, the angular difference between two-targets is calculated to $2.41°$.

Similarly, Fig.18(d) and (g) show the scenario when two targets are placed at the left and right side, respectively. Also, Fig.18(e) and (f) show the range profile and angle estimation for the left side case, and Fig.18(h) and (i) show and other images show the measurement results for each case. Even though SNR is little bit degraded due to the antenna pattern rather than the broadside case, the angular resolution is below than $3°$ for both left and right case. Specifically, two peak angles are derived to $-11.26°$ and $-8.38°$ (difference: $2.88°$) for the left case, $5.68°$ and $8.50°$ (difference: $2.82°$) for the right case.

C. TWO TARGETS FOR ELEVATION DIRECTION

The main difference between azimuth and elevation measurement is only the orientation of the platform. Since the platform is rotated to $90°$, the FoV is changed from $\pm 30°$ to $\pm 15°$. Fig.19 shows the measurement results for the elevation direction. Fig.19(a), (d) and (g) show the scenario when two targets were placed at broadside, left and right side, respectively and other images show the measurement results. Just like in the azimuth measurement result, the range profiles of the elevation measurement exhibit clutter by the horizontal post and protruded floor, and target scattering characteristics. However, in contrast to the azimuth, the range profile in the elevation direction appears to be slightly cleaner. This difference can be attributed to the dominant vertical polarization scattering characteristics present in the measurement environment. The angular estimation results demonstrate similar trends to those observed in the azimuth measurements. In the broadside case, two peak angles of $-1.23°$ and $1.66°$ are obtained, as shown in Fig.19(c). Likewise, for the left and right cases, two peak angles are estimated to $-10.85°$ and $-7.93°$, and $5.34°$ and $8.47°$, respectively, shown in Fig.19(f) and (i). The angular differences between the two targets are computed as $2.89°$, $2.92°$ and $3.13°$ for the broadside, left and right cases, respectively.

Upon a comprehensive examination of the diverse measurement outcomes, it can be affirmed that the angular resolution for both the azimuth and elevation directions has been successfully achieved with the IPCE technique,

TABLE 3. Algorithm computation Time [s].

	Proposed	MUSIC	BPDN
Azimuth	0.022	0.045	0.671
Elevation	0.020	0.031	0.592

measuring approximately 3° or less. Through these experimental results, the validity of the IPCE algorithm in co-prime array-based mmWave radar systems has been verified, and it can serve as a cornerstone for further research in radar systems aimed at high-resolution approaches.

D. COMPARISON WITH OTHER ALGORITHMS

In this paper, we evaluate the performance of the IPCE algorithm by comparing it with other angular estimation methods. We specifically compare it with commonly used high-resolution algorithms, such as the Multiple Signal Classification (MUSIC) algorithm [22] and one type of Compressed Sensing method known as Basis Pursuit Denoising (BPDN) [23]. The algorithm was executed on a PC equipped with an AMD Ryzen 5 5600X processor and 32GB of RAM. The algorithms were executed based on sampling with a 0.1° interval in both azimuth and elevation directions. Fig.20 presents the algorithm's results for each scenario, and Table 3 shows the time consumption for each algorithm's execution. Table 3 indicates that the IPCE algorithm is approximately twice as fast as the MUSIC algorithm and more than 29 times faster than the BPDN technique. This competitiveness is significant when considering the application of the algorithm in real-time systems, where it stands as a strong contender against other applicable algorithms.

VI. CONCLUSION

In this study, we have presented a novel approach to address the challenges of achieving high-resolution radar systems in the mmWave band, with a focus on applications in autonomous driving and automotive radar. By combining the co-prime array configuration with the TDM-MIMO technique, we successfully reduced the number of channels required while maintaining the desired angular resolution. The implementation of a W-band co-prime array and T/Rx chipsets based on the 65-nm CMOS process allowed for a one-to-one aperture coupling between the antenna and the chip, effectively reducing complexity and minimizing signal losses and phase deviations.

To overcome the issue of sidelobe effects for co-prime array, which can make it difficult to distinguish actual targets from ghost targets, we proposed the IPCE algorithm. Through iterative processing, the algorithm effectively identifies and eliminates sidelobe-induced signals, leading to improved target discrimination and more accurate angle estimation. The experimental results demonstrated the validity and effectiveness of our proposed approach. The high-resolution radar system achieved significant improvements in target detection and tracking capabilities, showcasing its potential for practical applications in autonomous driving and beyond.

ACKNOWLEDGMENT

(Taewoo Yu and Eunbin Kim contributed equally to this work.) The chip fabrication and EDA tools were supported by the IC Design Education Center (IDEC), South Korea.

REFERENCES

[1] J. Hasch, E. Topak, R. Schnabel, T. Zwick, R. Weigel, and C. Waldschmidt, "Millimeter-wave technology for automotive radar sensors in the 77 GHz frequency band," *IEEE Trans. Microw. Theory Techn.*, vol. 60, no. 3, pp. 845–860, Mar. 2012.

[2] C. Waldschmidt, J. Hasch, and W. Menzel, "Automotive radar—From first efforts to future systems," *IEEE J. Microw.*, vol. 1, no. 1, pp. 135–148, Jan. 2021.

[3] B. Sene, D. Reiter, H. Knapp, H. Li, T. Braun, and N. Pohl, "An automotive D-band FMCW radar sensor based on a SiGe-transceiver MMIC," *IEEE Microw. Wireless Compon. Lett.*, vol. 32, no. 3, pp. 194–197, Mar. 2022.

[4] P. Hügler, F. Roos, M. Schartel, M. Geiger, and C. Waldschmidt, "Radar taking off: New capabilities for UAVs," *IEEE Microw. Mag.*, vol. 19, no. 7, pp. 43–53, Nov. 2018.

[5] D. Bleh, M. Rosch, M. Kuri, A. Dyck, A. Tessmann, A. Leuther, S. Wagner, B. Weismann-Thaden, H.-P. Stulz, M. Zink, M. Riessle, R. Sommer, J. Wilcke, M. Schlechtweg, B. Yang, and O. Ambacher, "*W*-band time-domain multiplexing FMCW MIMO radar for far-field 3-D imaging," *IEEE Trans. Microw. Theory Techn.*, vol. 65, no. 9, pp. 3474–3484, Sep. 2017.

[6] J. Ziegler, "Making Bertha drive—An autonomous journey on a historic route," *IEEE Intell. Transp. Syst. Mag.*, vol. 6, no. 2, pp. 8–20, Summer 2014.

[7] J. Li and P. Stoica, "MIMO radar with colocated antennas," *IEEE Signal Process. Mag.*, vol. 24, no. 5, pp. 106–114, Sep. 2007.

[8] S. Sun, A. P. Petropulu, and H. V. Poor, "MIMO radar for advanced driver-assistance systems and autonomous driving: Advantages and challenges," *IEEE Signal Process. Mag.*, vol. 37, no. 4, pp. 98–117, Jul. 2020.

[9] A. Di Serio, P. Hugler, F. Roos, and C. Waldschmidt, "2-D MIMO radar: A method for array performance assessment and design of a planar antenna array," *IEEE Trans. Antennas Propag.*, vol. 68, no. 6, pp. 4604–4616, Jun. 2020.

[10] P. P. Vaidyanathan and P. Pal, "Sparse sensing with co-prime samplers and arrays," *IEEE Trans. Signal Process.*, vol. 59, no. 2, pp. 573–586, Feb. 2011.

[11] N. Amani, F. Jansen, A. Filippi, M. V. Ivashina, and R. Maaskant, "Sparse automotive MIMO radar for super-resolution single snapshot DOA estimation with mutual coupling," *IEEE Access*, vol. 9, pp. 146822–146829, 2021.

[12] P. Pal and P. P. Vaidyanathan, "Nested arrays: A novel approach to array processing with enhanced degrees of freedom," *IEEE Trans. Signal Process.*, vol. 58, no. 8, pp. 4167–4181, Aug. 2010.

[13] J. Liu, Y. Zhang, Y. Lu, S. Ren, and S. Cao, "Augmented nested arrays with enhanced DOF and reduced mutual coupling," *IEEE Trans. Signal Process.*, vol. 65, no. 21, pp. 5549–5563, Nov. 2017.

[14] W. Menzel and A. Moebius, "Antenna concepts for millimeter-wave automotive radar sensors," *Proc. IEEE*, vol. 100, no. 7, pp. 2372–2379, Jul. 2012.

[15] A. Bisognin, D. Titz, F. Ferrero, C. Luxey, G. Jacquemod, R. Pilard, F. Gianesello, D. Gloria, and P. Brachat, "Differential feeding technique for mm-wave series-fed antenna-array," *Electron. Lett.*, vol. 49, no. 15, pp. 918–919, Jul. 2013.

[16] M. Hrobak, "A modular MIMO millimeter-wave imaging radar system for space applications and its components," *J. Infr., Millim. THz Waves*, vol. 42, pp. 275–324, Nov. 2020.

[17] D. Schwarz, N. Riese, I. Dorsch, and C. Waldschmidt, "System performance of a 79 GHz high-resolution 4D imaging MIMO radar with 1728 virtual channels," *IEEE J. Microw.*, vol. 2, no. 4, pp. 637–647, Oct. 2022.

[18] M. Huan, J. Liang, Y. Wu, Y. Li, and W. Liu, "SASA: Super-resolution and ambiguity-free sparse array geometry optimization with aperture size constraints for MIMO radar," *IEEE Trans. Antennas Propag.*, vol. 71, no. 6, pp. 4941–4954, Mar. 2023.

[19] M. A. Richards, *Fundamentals of Radar Signal Processing*, 2nd ed. New York, NY, USA: McGraw-Hill, 2014.

[20] M. Q. Nguyen, R. Feger, J. Bechter, M. Pichler-Scheder, and A. Stelzer, "Comparing non-adaptive with adaptive windowing using multi-dimensional spatially variant apodization for automotive radar," in *Proc. 18th Eur. Radar Conf. (EuRAD)*, Apr. 2022, pp. 173–176.

[21] J.-S. Kim, H.-J. Kim, M. Shin, J.-H. Park, O.-Y. Kwon, R. Song, S. Lee, S. Nam, and B.-S. Kim, "79 GHz active array FMCW radar system on low-cost FR-4 substrates," *IEEE Access*, vol. 8, pp. 213854–213865, 2020.

[22] R. Schmidt, "Multiple emitter location and signal parameter estimation," *IEEE Trans. Antennas Propag.*, vol. AP-34, no. 3, pp. 276–280, Mar. 1986.

[23] S.-J. Kim, K. Koh, M. Lustig, S. Boyd, and D. Gorinevsky, "An interior-point method for large-scale l1-regularized least squares," *IEEE J. Sel. Topics Signal Process.*, vol. 1, no. 4, pp. 606–617, Dec. 2007.

TAEWOO YU received the B.S. degree in electronic and electrical engineering from Hongik University, Seoul, South Korea, in 2017. He is currently pursuing the combined M.S. and Ph.D. degree in electrical and computer engineering with Seoul National University, Seoul. His research interests include EM analysis, mmWave radar systems, and EM signal processing.

EUNBIN KIM received the B.S. degree in automobile engineering from Pyeongtaek University, Pyeongtaek, South Korea, in 2021, and the M.S. degree in electronic, electrical and computer engineering from Sungkyunkwan University, Suwon, South Korea, in 2023. She is currently a Research Engineer with the AD Sensor Research and Development Center, HL Klemove, Seongnam, South Korea. Her current research interests include mmWave circuit, automotive radar systems, and high-resolution radar systems.

JAE-HYUN PARK (Student Member, IEEE) received the B.S. degree in semiconductor systems engineering from Sungkyunkwan University, Suwon, South Korea, in 2016, where he is currently pursuing the Ph.D. degree in electronic, electrical and computer engineering. His current research interest includes millimeter-wave CMOS integrated circuit design for automotive radar systems.

BYUNG-SUNG KIM (Member, IEEE) received the B.S., M.S., and Ph.D. degrees in electronic engineering from Seoul National University, Seoul, South Korea, in 1989, 1991, and 1997, respectively. In 1997, he joined the College of Information and Communication Engineering, Sungkyunkwan University, Suwon, South Korea, where he is currently a Professor. He was a Visiting Researcher with the University of California at Santa Barbara, in 2013. His research interests include high-frequency device modeling and RF/millimeter-wave CMOS integrated circuit design.

SANGWOOK NAM (Senior Member, IEEE) received the B.S. degree in electrical engineering from Seoul National University, Seoul, South Korea, in 1981, the M.S. degree in electrical engineering from the Korea Advanced Institute of Science and Technology, Seoul, in 1983, and the Ph.D. degree in electrical engineering from The University of Texas at Austin, Austin, TX, USA, in 1989. From 1983 to 1986, he was a Researcher with the Gold Star Central Research Laboratory, Seoul. Since 1990, he has been a Professor with the School of Electrical Engineering and Computer Science, Seoul National University. His current research interests include analysis/design of electromagnetic structures, antennas, and microwave active/passive circuits.